Electronic and transport properties of armchair and zigzag sp^3-hybridized silicane nanoribbons

Jiseok Kim and Massimo V. Fischetti
Department of Materials Science and Engineering
University of Texas at Dallas
Richardson, TX 75080, USA
Email: jikim@ecs.umass.edu

Shela Aboud
Department of Energy Resources Engineering
Stanford University
Stanford, CA 94305, USA
Email: shelaa@stanford.edu

***Abstract*—The electronic and transport properties of sp^3-hybridized armchair and zigzag edge silicane nanoribbons have been investigated using nonlocal empirical pseudopotentials and $ab–initio$ calculations. Compared to the armchair graphene nanoribbons, silicane ribbons do no suffer from the chirality dependence of the band gap. Calculated low-field electron mobility and ballistic conductance show a strong edge dependence due to a difference in the effective masses and momentum relaxation rates along the transport direction. Smaller effective masses and momentum relaxation rates in the zigzag edge ribbons results in the electron mobility as much as an order of magnitude larger than the armchair edge ribbons.**

I. Introduction

Recent experiments have shown that possible growth of silicene stripes (silicene nanoribbons) – a silicon (Si) monolayer with two dimensional honeycomb lattice similar to graphene – on a Ag(110) substrate [1], [2] has attracted much attention due to its compatibility with conventional Si CMOS technology. Also, calculations of the binding energy of silicene using density function theory (DFT) has shown that the planar honeycomb structure is the least energetic configuration and is not stable unlike graphene sheets which are stable [3]. On the other hand, phonon dispersion studies have indicated that a low-buckled honeycomb structure of silicene is stable [3], and its electronic structures have shown very similar characteristics to graphene exhibiting closed gap and linear dispersion at the K-point [3], [4]. Upon hybridization of the silicene, also known as silicane, theoretical calculations have shown that sp^3-hybridization in low-buckled silicane structure is more stable and favorable than sp^2-hybridization both of which results in band gap opening [3], [5]–[7]. Also, it has been shown that the silicane is either a direct or indirect band gap semiconductor depending on the hybridized configurations (*i.e.* chair-like or boat-like) [5], [6], [8]. The chair-like configuration has hydrogen (H) atoms alternating above and below the Si layer while the boat-like configuration has H atoms alternating in pairs [6], [8]. It has been found that the chair-like configuration is always energetically lower than boat-like configuration [8].

A silicane nanoribbon (SiNR), the one dimensional silicane counterpart of graphene nanoribbon (GNR), can be classified into armchair and zigzag type depending on its edge shape (aSiNR and zSiNR, respectively). Interestingly, recent DFT calculations have shown the chirality dependence of the band gap in 'edge-only' H-passivated aSiNR with buckled configuration [3], [9] which was famously observed in armchair GNR (aGNR) [10]. However, electronic structures and the chirality dependence of the band gap of fully sp^3-hybridized SiNRs has not been conducted as well as the charge carrier transport properties in the SiNRs.

In this study, we investigate the electronic and carrier transport properties of fully sp^3-hybridized (chair-like) aSiNR and zSiNR. It should be clearly stated that we perform DFT calculations for the structural and electronic properties, and for the electronic properties we also employ the nonlocal empirical pseudopotentials (EPM) [11], [12] which is benchmarked to the results from the DFT calculation.

II. Crystal Structure and Geometry Relaxation

Figure 1 shows the atomic configuration of an aSiNR (a) and of a zSiNR (b); all Si dangling bonds, including those at the top and bottom of the monolayer surfaces, are passivated by hydrogen, thus causing the sp^3-hybridized bonding. The width of the SiNR is characterized by the number of Si-Si dimer lines or zigzag chains along the ribbon for the aSiNR or zSiNR, respectively, following the convention for graphene nanoribbons (GNRs) [10]. Note that we have used the unrelaxed atomic configuration when employing EPM while we have allowed relaxation to occur when using DTF. These two atomic configurations are shown in Fig. 2. The geometrical relaxation is performed as implemented in the Vienna *ab-initio* simulation package (VASP) [13], [14] using the conjugate gradient (CG) algorithm within the force-tolerance is set to 0.02 eV/Å and $1{\times}1{\times}8$ Monkhorst-Pack k-point grid is used. As seen in Fig. 2, the buckling height (represented as Δy) is reduced from $\Delta y = 0.784$ Å (uniform when unrelaxed) to $\Delta y_1 = 0.724$ Å and $\Delta y_1 = 0.739$ Å (buckling heights of inner Si-Si atoms and edge Si-Si atoms, respectively, after the relaxation) for the 4-zSiNR. However, there is not a noticeable variation of the buckling heights after relaxation depending on the width and edge shape of the ribbons.

III. Electronic Band Structure

For the electronic band structure calculation, we have employed the nonlocal EPM in which local pseudopotential $V(q)$

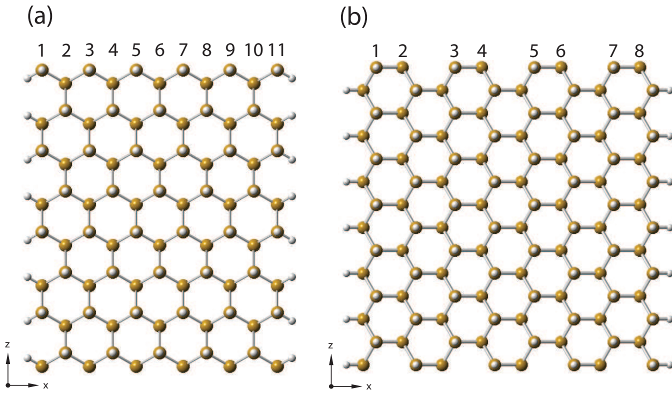

Fig. 1. Atomic configurations of (a) an 11-aSiNR and (b) an 8-zSiNR. All the Si (gold balls) dangling bonds are passivated by H (white balls). Note the H atoms passivate the dangling bonds in alternating pairs at the top and bottom sides of the monolayer.

for Si yields the correct value of the workfunction and of the energy gaps of the bulk band structure at high symmetry points [11]. The detailed calculation procedures of EPM can be found elsewhere [11], [12]. Due to the lack of the experimental data to benchmark the results from EPM, we have performed the DFT calculations as well using the VASP with a plane wave basis expansion and an energy cutoff of 450 eV. The electron-ion core interaction is represented by the projector augmented wave (PAW) [15] method and we have employed the Perdew-Burke-Ernzerhof (PBE) exchange correlation functional in the generalized gradient approximation (GGA) [16].

Electronic band structures for the aSiNRs and zSiNRs using EPM and DFT with both unrelaxed as well as fully relaxed geometry are shown in Fig. 3 where the relaxed geometry for EPM is obtained from the DFT calculation. The band structures from EPM show very similar characteristics to the DFT calculations exhibiting a direct band gap at Γ for 4-zSiNR and an indirect gap near the brillouin zone (BZ) edge for 7-aSiNR. However, the band gaps obtained from DFT are smaller than the EPM because of the well-known 'band gap underestimation problem' of DFT-GGA. Also, note that the energy dispersion from EPM is more dense than from DFT for the conduction bands for both zSiNR and aSiNR which

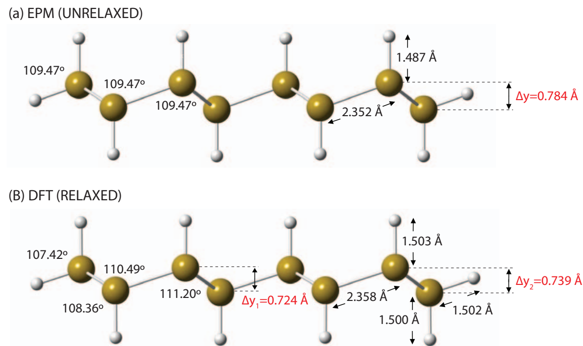

Fig. 2. Atomic configuration of an unrelaxed (a) and relaxed (b) 4-zSiNR for EPs and DFT calculations, respectively.

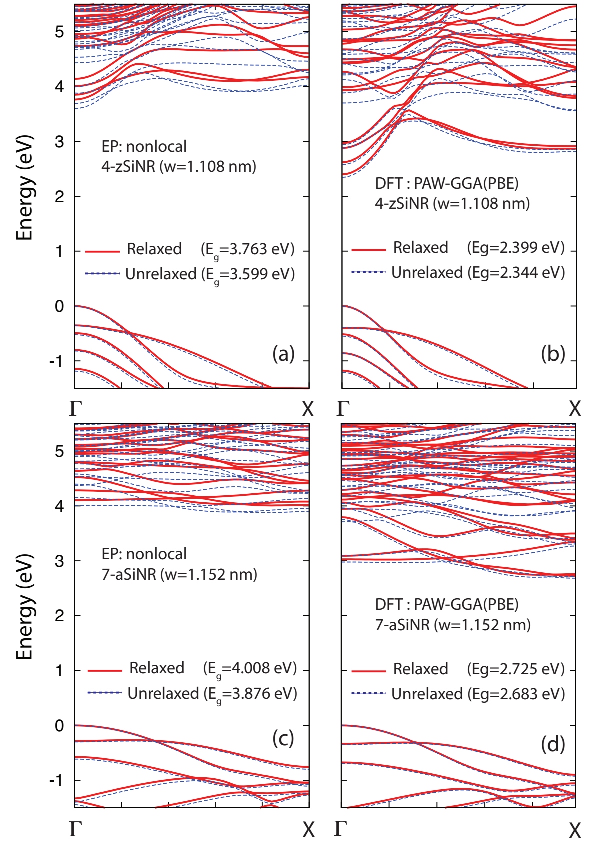

Fig. 3. Electronic band structure of a 4-zSiNR and 7-aSiNR using EPs [(a) and (c)] and DFT [(b) and (d)] with unrelaxed (dotted lined) and fully relaxed (solid line) geometry. The top of the valence bands are arbitrarily set to zero.

may be due to the different theoretical nature between EPM and DFT.

We show size dependence of the band gap for both aSiNR and zSiNR in Fig. 4 where the calculated band gaps from EP and DFT are represented as filled and open symbols, respectively. In contrast to the aGNR in Refs. [10], [17], the aSiNR does not show the chirality dependence of the band gap in both EP and DFT calculations. Instead, the band gap decreases nonlinearly as the ribbon width increases due to the quantum confinement effect, which is also in contrast to the 'edge-only' H-passivated aSiNR showing chirality dependence as shown in Refs. [3], [9]. This non-chirality dependence of the band gap of aSiNR is the result of the sp^3 bonding which ensures 4-fold coordination for all Si atoms and therefore it is not affected by the Clar resonances which control the edge structure in the sp^2 bonding of the aGNR.

IV. Transport Properties

In order to study electronic transport properties along the z-direction which is equivalent to the $[11\bar{2}]$ and $[10\bar{1}]$ for aSiNR and zSiNR, respectively, we calculate the ballistic conductances in SiNRs following Ref. [11] and the low-field electron mobility using the Kubo-Greenwood formula. We take into account for the electron-phonon scattering using the

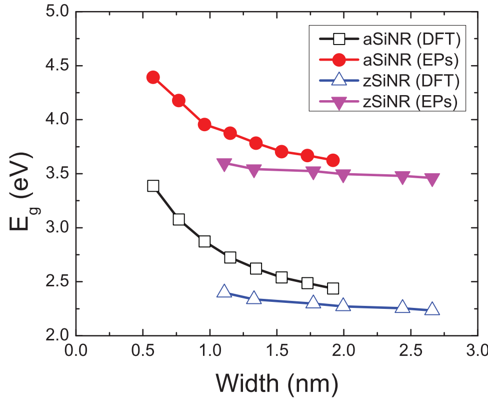

Fig. 4. Energy band gap as a function of ribbon width for aSiNR and zSiNR. Calculated band gaps using EPs and DFT are represented as filled and open symbols, respectively.

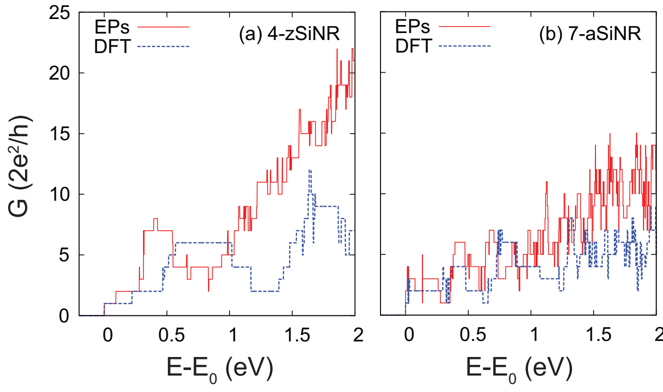

Fig. 5. 1D ballistic conductance for 4-zSiNR and 7-aSiNR where the conduction band edge E_0 is referenced to zero. Calculated ballistic conductances using EPs and DFT are represented as solid and dotted lines, respectively.

bulk Si deformation potentials. Fig. 5 shows the calculated ballistic conductances in units of the quantum conductance $G_0 = 2e^2/h$ for the 4-zSiNR (w=1.108 nm) and 7-aSiNR (w=1.152 nm) using both EPM and DFT where the conduction band edge E_0 is referenced to zero. As clearly seen, the conductance is larger in 4-zSiNR than in 7-aSiNR using both EPM and DFT due to the fewer Landauer channels in 7-aSiNR. The one dimensional (1D) low-field electron mobility along the z-direction is given as,

$$\mu_{zz} = \frac{1}{n_l}\sum_{\alpha} n^{(\alpha)}\mu_{zz}^{(\alpha)} \tag{1}$$

where α represents the conduction band index, n_l and $n^{(\alpha)}$ represent the electron line density and electron density at subband α, respectively. The mobility tensor $\mu_{zz}^{(\alpha)}$ is given as,

$$\begin{aligned}\mu_{zz}^{(\alpha)} &= \frac{2e}{\hbar n^{(\alpha)}}\sum_{k_z} v_z^{(\alpha)}(k_z)\tau_{tot,z}^{(\alpha)}(k_z)\frac{\partial f_0(E^{(\alpha)}(k_z))}{\partial k_z} \\ &= \frac{e}{k_bT\pi n^{(\alpha)}}\int dk_z v_z^{(\alpha)}(k_z)v_z^{(\alpha)}(k_z)\tau_{tot,z}^{(\alpha)}(k_z) \\ &\times f_0(E^{(\alpha)}(k_z))\left[1 - f_0(E^{(\alpha)}(k_z))\right]\end{aligned} \tag{2}$$

where $v_z^{(\alpha)}(k_z) = (1/\hbar)dE^{(\alpha)}(k_z)/dk_z$ and $f_0(E^{(\alpha)}(k_z))$ are group velocity and the distribution function at equilibrium (Fermi–Dirac), respectively. The total momentum relaxation rate $1/\tau_{tot,z}^{(\alpha)}(k_z)$ is given as,

$$\frac{1}{\tau_{tot,z}^{(\alpha)}(k_z)} = \frac{1}{\tau_{ac,z}^{(\alpha)}(k_z)} + \frac{1}{\tau_{op(ab),z}^{(\alpha)}(k_z)} + \frac{1}{\tau_{op(em),z}^{(\alpha)}(k_z)} \tag{3}$$

where $\tau_{ac,z}^{(\alpha)}(k_z)$, $\tau_{op(ab),z}^{(\alpha)}(k_z)$, and $\tau_{op(em),z}^{(\alpha)}(k_z)$ are the relaxation time due to the scattering between electrons and bulk acoustical, optical (absorption and emission) phonons, respectively. The momentum relaxation rates, assuming non-polar, elastic, and isotropic scattering and using equipartition approximation, can be written as,

$$\frac{1}{\tau_{ac,z}^{(\alpha)}(k_z)} = \frac{2\pi}{\hbar}|V_{ac}|^2\sum_{k_z',\alpha'} F_{k_z,k_z',\alpha,\alpha'}\delta\left[E^{(\alpha)}(k_z) - E^{(\alpha')}(k_z')\right] \tag{4}$$

where the electron and phonon momentum independent $|V_{ac}|^2 = (\Delta_{ac}^2 k_B T)/(2\rho v_s^2)$ for acoustic phonons with bulk Si acoustic phonon deformation potential $\Delta_{ac} = 5.8$ eV [18], crystal mass density $\rho = 2.33\times10^{-3}$ kg/cm^3 [19], and sound velocity $v_s = 9.20\times10^5$ cm/s [20]. Similarly, for optical phonons,

$$|V_{op}|^2 = \frac{(D_tK)_{op}^2\hbar}{2\rho w_{op}}\left\{\begin{array}{l} n_{op} \\ n_{op}+1 \end{array}\right\} \quad \begin{array}{l}\text{(absorption)} \\ \text{(emission)}\end{array} \tag{5}$$

where we use optical phonon deformation potential $(D_tK) = 2.6\times10^8$ eV/cm [18], optical phonon energy $\hbar w_{op} = 61.2\times10^{-3}$ eV [19], and phonon occupation number $n_{op} = 1/(e^{\hbar w_{op}/k_BT}-1)$. The overlap integral $F_{k_z,k_z',\alpha,\alpha'}$ considering only N-processes ($i.e.$ $G_z = 0$) is,

$$F_{k_z,k_z',\alpha,\alpha'} = \int d\vec{R}|\zeta_{k_z'}^{(\alpha')*}(\vec{R})|^2|\zeta_{k_z}^{(\alpha)}(\vec{R})|^2 \tag{6}$$

where the two dimensional wavefunction $\zeta_{k_z}^{(\alpha)}(\vec{R})$ is given as,

$$\zeta_{k_z}^{(\alpha)}(\vec{R}) = \frac{1}{A^{1/2}}\sum_{\vec{G}_\parallel} u_{G_z=0,\vec{G}_\parallel,k_z}^{(\alpha)}(\vec{R})e^{i\vec{G}_\parallel\cdot\vec{R}} \tag{7}$$

where the $\vec{G}_\parallel$ and $\vec{R}$ represent in-plane reciprocal and direct lattice vectors, respectively, and A is the normalization area of the two dimensional plane ($i.e.$ x-y plane of the unit cell in Fig.1). We evaluate the electron mobility using the eigen–energies and Bloch functions calculated from the EPM. Fig. 6 and Fig. 7 show the total momentum relaxation rates at a given line density and the electron mobility as a function of the line density, respectively, for the 4-zSiNR and 7-aSiNR. The electron mobility is more than 20 times larger for the 4-zSiNR (∼500 cm^2/Vs) than the 7-aSiNR (∼23 cm^2/Vs) as shown in Fig. 7 (a). This dramatic increase of the electron mobility for the 4-zSiNR can be ascribed to the smaller band gap so the smaller effective mass, higher group velocity per axial crystallographic orientation, and lower momentum relaxation rates near the conduction band edges as shown in Fig. 6 due to the smaller overlap integral. The width dependence of the mobility is shown in Fig. 7 (b) at a line density

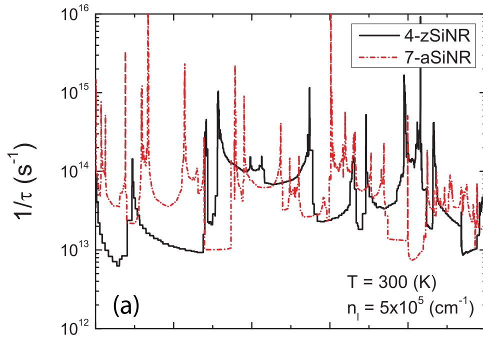

Fig. 6. Electron-phonon momentum relaxation time accounting for the acoustic, optical emission and optical absorption scattering for 4-zSiNR (solid lines) and 7-aSiNR (dashed lines) at the line density $n_l = 5 \times 10^5$ cm^{-1} and the temperature $T = 300$ K.

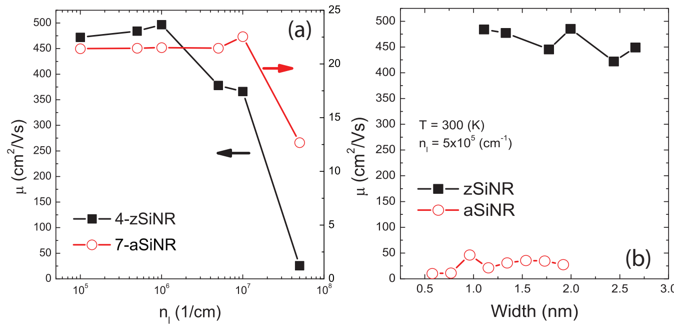

Fig. 7. Electron mobility as a function of the line density n_l for 4-zSiNR (filled symbols) and 7-aSiNR (open symbols).

($n_l = 5 \times 10^5$ cm^{-1}) and temperature ($T = 300$ K). As seen, the electron mobility is not as smooth as effective–mass approximation because of the full band structure effect which causes the switching of the effective masses at the bottom of the subband due to the band crossing. Note that the electron mobility for the 4-zSiNR ($\sim$500 cm^2/Vs) is comparable to the experimental measurement for the multichannel GNRFET (50 $\sim$ 200 cm^2/Vs with width 1$\sim$3 nm) [21].

V. Conclusions

In conclusion, we have investigated the structural, electronic, and transport properties of sp^3-hybridized (chairlike) aSiNRs and zSiNRs. DFT calculations show both sp^3-hybridized aSiNRs and zSiNRs are stable in buckled configuration. Electronic band structures using EPM are very comparable to the DFT except the band gap. Both EPM and DFT predict direct and indirect gap for zSiNRs and aSiNRs, respectively, and the band gap shows no chirality dependence with ribbon width for both aSiNRs and zSiNRs. Finally, we show a strong edge shape dependence on the ballistic conductance and low-field electron mobility, both of which are much larger in zSiNRs.

Acknowledgment

The authors gratefully acknowledge the support by SRC, MARCO/MSD, FCRP, Texas Instrument, and Samsung Electronics Co., Ltd..

References

[1] A. Kara, C. Léandri, M. Davila, P. De Padova, B. Ealet, H. Oughaddou, B. Aufray, and G. Le Lay, "Physics of silicene stripes," *J. Supercond. Novel Magn.*, vol. 22, no. 3, pp. 259–263, 2009.

[2] B. Aufray, A. Kara, S. Vizzini, H. Oughaddou, C. Léandri, B. Ealet, and G. Le Lay, "Graphene-like silicon nanoribbons on ag (110): A possible formation of silicene," *Appl. Phys. Lett.*, vol. 96, p. 183102, 2010.

[3] S. Cahangirov, M. Topsakal, E. Aktürk, H. Şahin, and S. Ciraci, "Two- and one-dimensional honeycomb structures of silicon and germanium," *Phys. Rev. Lett.*, vol. 102, p. 236804, 2009.

[4] H. Şahin, S. Cahangirov, M. Topsakal, E. Bekaroglu, E. Akturk, R. Senger, and S. Ciraci, "Monolayer honeycomb structures of group-iv elements and iii-v binary compounds: First-principles calculations"," *Phys. Rev. B*, vol. 80, no. 155453, 2009.

[5] T. Osborn, A. Farajian, O. Pupysheva, R. Aga, and L. Voon, "Ab initio simulations of silicene hydrogenation," *Chem. Phys. Lett.*, vol. 511, pp. 101–105, 2011.

[6] M. Houssa, E. Scalise, K. Sankaran, G. Pourtois, V. Afanas'ev, and S. A., "Electronic properties of hydrogenated silicene and germanene," *Appl. Phys. Lett.*, vol. 98, no. 22, pp. 223 107–223 107–3, 2011.

[7] G. Guzmán-Verri and L. Voon, "Electronic structure of silicon-based nanostructures," *Phys. Rev. B*, vol. 76, p. 075131, 2007.

[8] L. Voon, E. Sandberg, R. Aga, and A. Farajian, "Hydrogen compounds of group-iv nanosheets," *Appl. Phys. Lett.*, vol. 97, no. 16, p. 163114, 2010.

[9] S. Cahangirov, M. Topsakal, and S. Ciraci, "Armchair nanoribbons of silicon and germanium honeycomb structures," *Phys. Rev. B*, vol. 81, p. 195120, 2010.

[10] Y.-W. Son, M. L. Cohen, and S. G. Louie, "Energy gaps in graphene nanoribbons," *Phys. Rev. Lett.*, vol. 97, p. 216803, 2006.

[11] J. Kim and M. Fischetti, "Empirical pseudopotential calculations of the band structure and ballistic conductance of strained [001],[110], and [111] silicon nanowires," *J. Appl. Phys.*, vol. 110, p. 033716, 2011.

[12] J. Kim and M. Fischetti, "Electronic band structure calculations for biaxially strained si, ge, and iii-v semiconductors," *J. Appl. Phys.*, vol. 108, p. 013710, 2010.

[13] G. Kresse and J. Hafner, "Ab initio molecular dynamics for liquid metals," *Phys. Rev. B*, vol. 47, no. 1, p. 558, 1993.

[14] G. Kresse and J. Furthmüller, "Efficient iterative schemes for ab initio total-energy calculations using a plane-wave basis set," *Phys. Rev. B*, vol. 54, no. 16, p. 11169, 1996.

[15] G. Kresse and D. Joubert, "From ultrasoft pseudopotentials to the projector augmented-wave method," *Phys Rev B*, vol. 59, no. 3, p. 1758, 1999.

[16] J. Perdew, K. Burke, and M. Ernzerhof, "Generalized gradient approximation made simple," *Phys. Rev. Lett.*, vol. 77, no. 18, pp. 3865–3868, 1996.

[17] L. Yang, C. Park, Y. Son, M. Cohen, and S. Louie, "Quasiparticle energies and band gaps in graphene nanoribbons," *Phys. Rev. Lett.*, vol. 99, no. 18, p. 186801, 2007.

[18] M. Fischetti, N. Sano, S. Laux, and K. Natori, "Hole-initiated impact ionization and split-off bands in ge, si, gaas, inas, and ingaas," in *Proc. Int. Workshop Comp. Electron. (IWCE6)*, 1998.

[19] M. Fischetti and S. Laux, "Band structure, deformation potentials, and carrier mobility in strained si, ge, and sige alloys," *Journal of Applied Physics*, vol. 80, p. 2234, 1996.

[20] M. Fischetti and S. Laux, "Monte carlo study of electron transport in silicon inversion layers"," *Phys. Rev. B*, vol. 48, no. 4, pp. 2244–2274, 1993.

[21] X. Wang, Y. Ouyang, X. Li, H. Wang, J. Guo, and H. Dai, "Room-temperature all-semiconducting sub-10-nm graphene nanoribbon field-effect transistors"," *Phys. Rev. Lett.*, vol. 100, no. 20, 2008.